

Application of reconfigurable pinhole mask with excimer laser to fabricate microfluidic components

Kevin Conlisk · Sébastien Favre · Theo Lasser · Gerard M. O'Connor

Received: 23 November 2010 / Accepted: 8 December 2010 / Published online: 6 January 2011
© Springer-Verlag 2010

Abstract An excimer laser incorporating a reconfigurable intelligent pinhole mask (IPM) is demonstrated for the fabrication of microfluidic geometries on a poly(methyl methacrylate) substrate. Beam reconfiguration techniques are used to overcome some of the drawbacks associated with traditional scanning laser ablation through a static mask. The production of zero lead-in (ZLI) features are described, where the ramp lead-in angle—inherent to scanning laser ablation—is reduced to be in line with the cross-sectional side-wall angle of the microchannel itself. The technique is applied to eliminate under-cutting and ramping at channel junctions—features resulting from scanning ablation through a fixed mask—and produce flat crossing sections, junctions and inlets. The development of a prediction model for microchannel visualisation and refinement prior to the fabrication step is also described. The model includes variables from the IPM, laser, scanning stage and material etch rate allowing quantitative measurement of generated microchannel geometry. One application of the model is the development of microchannel mixing geometry which is analysed using computational fluid dynamic (CFD) techniques. For this purpose, the effect

of varying the overall channel geometry on mixing within a microchannel was investigated for flows with low Reynolds numbers. The resulting geometry is found to reduce the distance required for mixing by 50% in comparison to a straight planar channel, thereby enabling smaller device geometries.

Keywords Excimer laser · Intelligent pinhole mask · Microfluidic mixer · Prediction model · PMMA

1 Introduction

Initial techniques used to fabricate microfluidic devices emerged from the electronics sector due to the similarities of lab-on-chips with integrated circuits. First devices were fabricated on glass or silicon substrates using photolithography steps (Chong and Jin-Woo 2004). This meant the process was expensive and so the industry turned to polymers due to their relatively cheap production costs which allowed the development of disposable microfluidics. Becker and Gartner presented a comprehensive overview of polymer microfabrication technologies (Becker and Gartner 2008). Injection moulding and hot embossing were identified as some of the best replication techniques. Their advantages lie in the fact that they can produce high quality, low cost microfluidic devices on a large scale. However, these techniques are inherently unsuitable for rapid prototyping, when you consider the number of iterative design changes that may be required and the complexity of master fabrication. Therefore, alternative methods for the rapid production of high quality microfluidic prototypes are needed.

Many groups involved in fabricating microfluidics and microfluidic mixers use a polymer casting technique

K. Conlisk (✉) · G. M. O'Connor
National Centre for Laser Applications, School of Physics,
National University of Ireland Galway, University Road,
Galway, Ireland
e-mail: kevin.conlisk@nuigalway.ie

S. Favre
Swiss Manufacturing Operation, Medtronic, Switzerland
e-mail: sebastien.favre@mac.com

T. Lasser
BM 5143 (Btiment BM), Station 17, 1015 Lausanne,
Switzerland
e-mail: theo.lasser@epfl.com

(Chung and Shih 2008; Bhagat et al. 2007; Shim et al. 2007; Shih and Chung 2007; Stroock et al., 2002). A master mould is created by exposing a silicon wafer coated in SU-8 resist through a photomask. PDMS is then cast over the mould to replicate the channel geometries. It is a time consuming process which again does not lend itself well to iterative device changes. Some groups have sought to overcome the cost and complexity associated with the master fabrication step by using printed circuit boards (PCB) or laser printed transparencies as masters. Abdelgawad et al. (2008) printed the microchannel layout directly onto a PCB. The un-coated copper was etched away to leave a master for casting. Li et al. (2006) exposed a resist-coated PCB through a thermally printed photomask to create a master. In both cases, PDMS was cast over the PCB master to create a microfluidic device. Channel widths are on the order of hundreds of microns. Tan et al. (2001) used a laser printed transparency directly as a master substantially reducing the fabrication time. The depth of the toner deposited on the transparency defined the channel depth. Other groups have demonstrated similar techniques (Liu et al. 2005; Lucio do Lago et al. 2003). The limiting factor for these methods is the channel depth, defined by the depth of toner printed on the films, which is less than 20 μm . Although useful for prototyping simple devices the feature resolution, quality and reproducibility is inherently poor using these techniques. However, other rapid prototyping methods based on laser ablation offer a greater level of precision, control and repeatability.

Thermoplastic polymers, such as poly(methyl methacrylate) (PMMA), can be directly machined by a laser eliminating the need for an expensive master. There are numerous examples in the literature of laser processing of polymers for microfluidic applications. Khan Malek presented a two-part overview on the topic (Khan Malek 2006a, b). The review highlighted certain advantages of laser processing as a fabrication tool. These include, precision, speed—compared to fabricating a master, complex geometries, localised materials processing with minimal effect on the overall part and no special requirements such as a clean room or wet etching facilities. CO_2 lasers (Klank et al. 2002; Pflöging et al. 2009; Hong et al. 2010), diode-pumped solid-state (DPSS) lasers (Yoshida 2007; Lim et al. 2003) and excimer lasers (Yoshida 2007; Waddell et al. 2002; Roberts et al. 1997; Heng et al. 2006) have all been demonstrated to produce microfluidics. However, the process can have certain drawbacks including variations in channel width, depth and shape when producing complex geometries. When trying to make a process comparable to mass production techniques certain areas such as where channels meet, intersect, change direction or diameter need special consideration.

Excimer mask projection techniques used to produce more complex structures have been discussed previously (Gower 1999; Rizvi 1999). These range from static step-and-repeat to workpiece dragging, mask dragging and synchronised overlay scanning. Traditionally, in mask projection machining the processing mask has a smaller aperture than the overall beam size. However, in some techniques used to produce more complex geometries, a mask, with predefined areas of transparency and opacity, which is larger in area in comparison to the excimer beam size is used. The mask and substrate movement are synchronised in order to produce the desired result. Half-tone or greyscale masks can also be used to produce features of varying depth. The drawback with these techniques is the requirement to fabricate a mask of predefined transparency, shape or size before it can be used with the laser to produce the desired geometry.

This work is based around the use of an excimer laser and intelligent pinhole mask (IPM). Using this reconfigurable mask some of the drawbacks associated with scanning laser ablation are overcome. We demonstrate the production of zero lead-in (ZLI) features which are used to fabricate flat channel intersections, inlets and corners. By eliminating the need for a master-mask, the complexity of the process is reduced. We use this platform to create micromixing geometries that would be difficult to fabricate with traditional static mask techniques. This includes the development of a LabVIEW based prediction model to visualise and allow for refinement of the mixer geometry prior to the fabrication step. We carry out computational fluid dynamic (CFD) analysis of the resulting structures to provide quantitative feedback on their performance.

2 Experimental

2.1 Laser workstation and IPM

For this work, an excimer laser (ATLEX-SPI, ATL, Germany) employing an argon–fluoride gain medium and lasing at 193 nm was utilised. It has a maximum repetition rate of 300 Hz and typical fluence, ϕ (energy per unit area), values at the sample are in the region of 0.1–5 J cm^{-2} . The laser is integrated with a laser workstation (MicroMaster, Optec, Belgium) which houses an opto-mechanical beam delivery module. This provides control over the scanning stages and demagnification optics. The stages are TTL pulse stages with a positional resolution of 1 μm in both the X- and Y-axis. A demagnification ratio of between 4 and 11.5 is achievable using a 3 element lens (3e-lens). The raw beam exiting the cavity is 5 \times 2 mm in size and is used directly for mask projection machining. The only

physical change to this workstation is the replacement of the static mask with the IPM—depicted in Fig. 1.

The IPM is a dynamic mask comprising of four adjustable blades and was originally developed for microscopy applications. However, as this is its first application towards laser machining some of the main points of the IPM will be highlighted; the reader is directed toward Sidler et al. (2004) for a more comprehensive overview on the IPM’s construction and operation. The blades are fabricated from silicon and mounted on base-plates which are controlled by magnetic actuators. Two sets of blades are placed on top of each other with one set rotated by 90° to realize a four blade aperture. The result is a rectangular aperture of programmable area with a maximum areal expansion of ~1 mm². Each blade can be programmed individually through a LabVIEW (National Instruments, UK) graphical user interface (GUI). The IPM blade movement is synchronised with the laser operation to facilitate a highly controlled and repeatable process. Each blade can be positioned with a 30 nm repeatability. The minimum feature size achievable is defined by the controlling voltage on the IPM blades, the resulting opening can be as small as a few microns. The limiting factor in this case is the fluence when using such a small mask may not be sufficient to achieve ablation. For the purposes of this work channel widths of 100 µm were selected as this is in line with current trends.

The LabVIEW GUI allows for control of the movement of the IPM during the laser machining process. In its

simplest operation it can be used as a square mask where a displacement is applied to each blade. However, the novelty of the system lies in the ability to arbitrary control the position of each mask blade, in real time, during the fabrication process. For example, this can take the form of an applied triangle, sawtooth, square or sine waveform, whose phase, offset, frequency and amplitude can also be controlled. The complexity of the IPM operation coupled with the laser parameters and scanning stage renders it difficult to predict channel geometries when using a large array of inputs. This has led to the need for a model to visualise, and subsequently refine, channel geometry prior to fabrication.

Characterisation of the ablated structures was carried out by scanning electron microscope (SEM, Phenom, FEI, USA), white-light profilometer (NewView 100, Zygo, USA) for channel depth measurements and an optical microscope (Olympus, Japan) for surface measurements. The optical microscope has a mechanical X/Y stage linked to a digital display with a resolution of 5 µm

2.2 Prediction model

The prediction model is based on array algebra. The surface of the material to be ablated and the area of the IPM are defined as arrays. Each $m \times n$ array has a resolution of 1 µm in both the X and Y direction. The ratio of substrate scan velocity (v_s) to laser frequency (f) gives the incremental distance between laser pulses. This allows the calculation of the position of the IPM above the surface. The IPM array contains etch rate data which is related to the laser fluence and material properties. For each laser pulse the position and size of the re-imaged IPM mask is calculated. The height of the exposed area of the surface array is decremented according to the etch rate.

The number of laser pulses at a distance x along the microchannel, where $x > M_L$, is calculated using the following relationship

$$NP_x = \frac{M_L \times f}{v_s}, \tag{1}$$

where M_L is the demagnified mask length in the direction of motion of the X/Y stage, f the laser frequency and v_s the substrate scan velocity in the x direction along the length of the microchannel. The channel depth, d_{ch} , can then be estimated by considering the etch rate, r , of the material under ablation.

$$d_{ch} = NP_x \times r. \tag{2}$$

Table 1 contains a list of the process variables used. The initial inputs to the system allow the calculation of the fluence at the workpiece which in turn sets up the IPM

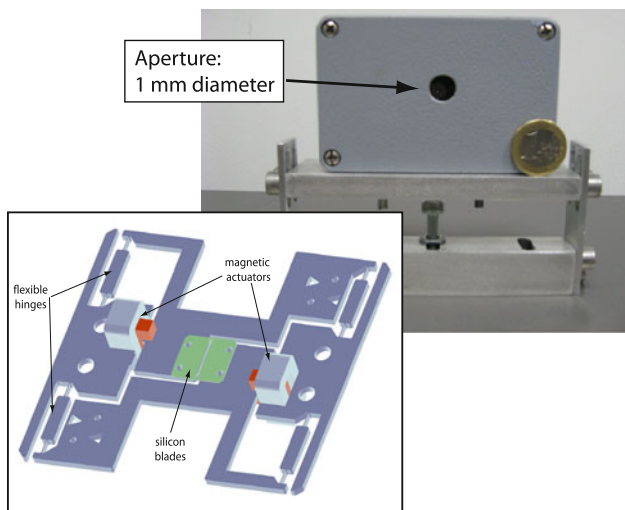


Fig. 1 The intelligent pinhole mask (IPM) and schematic showing one set of pinhole blades. The blades, and associated control electronics, are housed within the grey protective casing which is mounted on a bracket making it possible to secure the mask on the MicroMaster workstation. The aperture to pass the laser light measures 1 mm in diameter. A one euro coin is shown for scale

Table 1 Prediction model variables. The variables in ‘Mask select’ may be unique to each IPM blade

Initial inputs	Mask select	Laser parameters
Pulse energy	Offset	Frequency
Mask length	Waveform	Scan velocity
	Amplitude	Scan distance
	Frequency	Scan direction
	Phase	

array with etch rate data. The mask properties for the scan are selected along with laser parameters such as frequency, velocity, distance and direction. In the mask select process alone there are 20 variables, emphasising the need for a prediction model. The model allows visualisation of microchannel geometry and quantitative measurement of channel width and depth. The geometry may also be exported for use in computational fluid dynamic analysis software. In this way different design iterations may be assessed quickly reducing the number of trial devices.

2.3 CFD analysis

Computational fluid dynamics (CFD) analysis was carried out using COMSOL Multiphysics (COMSOL, Sweden). Certain assumptions are proposed in this work, such as, steady state flow is established at the inlets, no-slip boundary conditions at channel walls and body force does not influence the simulation results. It is also assumed that no chemical reaction takes place between the fluids entering the microchannels and that the channels themselves are smooth, free from any experimental imperfections.

During the analysis the continuity equation, (3), and Navier–Stokes equation, (4), are solved in the case of an isothermal incompressible fluid:

$$\nabla \cdot u = 0 \quad (3)$$

$$\rho u \cdot \nabla u = -\nabla p + \eta \nabla^2 u \quad (4)$$

where u is the velocity vector, p the pressure and η the dynamic viscosity of the fluid. The distribution of the species concentration is obtained by solving the diffusion–convection equation, (5), where the velocity vectors calculated in Eqs. 3 and 4 are used as input parameters.

$$\nabla \cdot (-D\nabla c_s) = u \cdot \nabla c_s \quad (5)$$

Here D is the diffusion coefficient of the species and c_s is the species concentration. For the simulations in this work values of $D = 1 \times 10^{-10} \text{ m}^2 \text{ s}^{-1}$, $\rho = 1 \times 10^3 \text{ kg m}^{-3}$ and $\eta = 1 \times 10^{-3} \text{ kg m}^{-1} \text{ s}^{-1}$ were selected. These values are representative of water at 20°C

3 Results and discussion

3.1 Fabricating microchannels

One of the major drawbacks to scanning laser ablation through a static mask is the production of ramped lead-in and lead-out features on microchannels. Figure 2 shows schematically the relationship between mask length, M_L , ramp length, L_r and corresponding ramp angle, θ_r . It is clear that the length of the mask in the direction of movement of the X/Y stage will determine the length of both the lead-in and lead-out ramps. The ramp angle, is related to the depth of the microchannel, d_{ch} , and can be calculated from the following expression: $\theta_r = \tan^{-1}(L_r/d_{ch})$.

The presence of this ramp during scanning laser ablation makes it difficult to accurately reproduce complex microchannel networks. For example, to join two perpendicular microchannels with minimal overlap would require either a small θ_r or L_r . For the former—considering the use of a static mask measuring $100 \mu\text{m} \times \mu\text{m}$ —it would require a microchannel with a depth greater than $500 \mu\text{m}$. Not only would this depth of channel be difficult to fabricate, but it may not meet the requirements of the particular application. For the latter, to have an appropriately small L_r , would require an equally small M_L —which is technically not feasible for realistic throughput. Both cases assume $\theta_r \sim 10^\circ$ is sufficient to provide the minimal overlap required.

Figure 3 shows CAD images of possible geometries when trying to create a corner junction in a microfluidic device using a static mask. In Fig. 3a the junction is over-etched where the ends of both microchannels meet. At its deepest point, the depth of the over-etch, d_{oe} , is related to the depth of the channel, d_{ch} , by $d_{oe} \sim 2 \times d_{ch}$. To reduce the length of the over-etch the two channels may be offset,

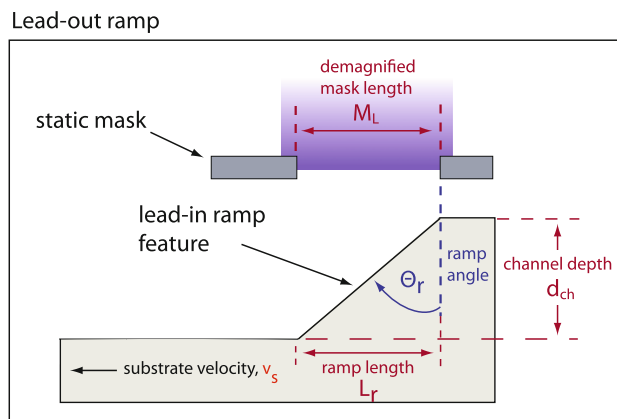


Fig. 2 Schematic diagram of the lead-out ramp formed at the end of a microchannel when using scanning laser ablation and a static mask. Demagnified mask length, M_L , ramp length, L_r and ramp angle, θ_r , measurements are indicated

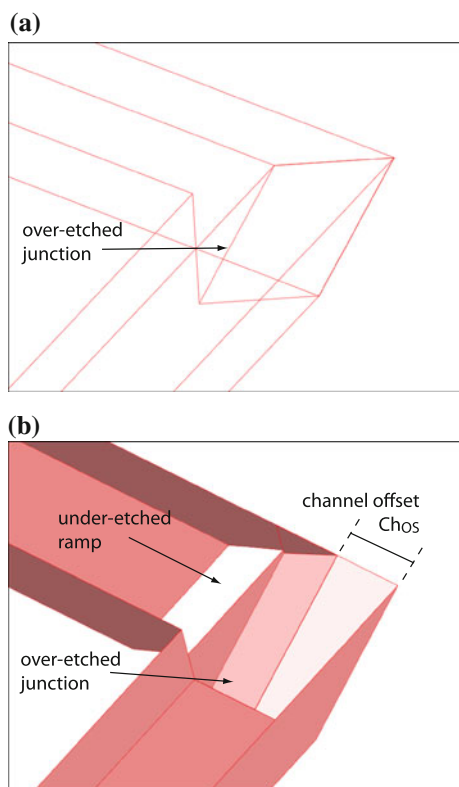


Fig. 3 CAD images depicting possible junction geometries when using scanning laser ablation through a static mask. **a** An over-etched junction. **b** An under-etched junction showing the addition of a ramp at the entrance to the second channel. Over-etched regions increase the likelihood of dead volumes at these junctions while under-etched junctions result in an increased pressure drop

however, the resulting geometry will now include a ramp at the entrance to the second channel—Fig. 3b. The ramp height, h_r , is related to the channel offset, Ch_{os} , and ramp angle, θ_r , by $h_r = Ch_{os} / \tan \theta_r$.

The result of these non-flat junctions—Fig. 3a, b—can lead to the creation of dead-volumes. This area may be reduced by increasing the Ch_{os} . However, there is a trade-off between reduction in dead-volume and increase in pressure-drop across the junction. For channels with zero offset, such as Fig. 3a, the increase in dead-volume is offset by a lower pressure drop. On trying to reduce the dead-volume by increasing the Ch_{os} , such as in Fig. 3b, the result will be a ramp at the entrance to the second channel. The production of this ramp is then responsible for an increase in pressure-drop across the junction. An increase in pressure-drop can be detrimental in cascading style systems, where a number of junctions may be present.

To effectively join two microchannels, for low pressure-drop and dead-volume, requires a small θ_r . This can be achieved with the IPM using developed beam reconfiguration techniques. ZLI features are achievable by appropriately controlling the position of the mask blades during

the machining process. Figure 4 outlines the ZLI technique to eliminate the ramped lead-in and lead-out to a microchannel. The frequency, f_b , which the blade must be opened at to produce the ZLI is related to the substrate velocity, v_s , and demagnified mask length, M_L , by

$$f_b = \frac{v_s}{2M_L} \tag{6}$$

Figure 5 shows a comparison of θ_r for channels machined with a static— $100 \mu\text{m} \times 100 \mu\text{m}$ —mask and the IPM using the ZLI technique. The laser parameters were, $f = 50 \text{ Hz}$, $\phi = 150 \text{ mJ cm}^{-2}$ and v_s varied from $10\text{--}50 \mu\text{m s}^{-1}$. Included in the graph is cross-sectional sidewall angle measurements for each microchannel for comparison to the ZLI θ_r . From the graph it can be seen that θ_r for the ZLI technique is approximately equal to the sidewall angle. The sidewall angle was used for comparative reasons as this gives the best indication of the minimum taper achievable given a particular fluence and set of machining parameters. This allows the application of the technique to produce more complex geometries, such as, where channels intersect.

This technique can be applied to eliminate the drawbacks to traditional scanning laser ablation as seen in Fig. 3. Figure 6 shows how junction undercutting and ramping may be eliminated to produce flat intersections on corners, crossing channels and inlets. The channels were fabricated with laser and IPM parameters of $f = 50 \text{ Hz}$, $\phi = 200 \text{ mJ cm}^{-2}$, $v_s = 20 \mu\text{ms}^{-1}$, $M_L = 100 \mu\text{m}$ and $f_b = 0.1 \text{ Hz}$. The ZLI technique is used as a building block to fabricate more complex geometries and ultimately microfluidic devices. The following sections will look at the prediction model validation and micromixer generation and analysis.

3.2 Prediction model validation

Experimentally obtained calibration curves are used to model the laser, IPM and material response. It was noted that increasing f or reducing the demagnification ratio will reduce the fluence on the sample and hence the etch rate per pulse. Individual voltage–displacement curves for each IPM blade were used to accurately characterise its response to both a negative and positive voltage bias. Each blade required a separate 2nd order polynomial fit ($R^2 = 0.99$ in all cases) to allow for accurate control of the blade aperture size. Finally, the response of the material—in this case PMMA—to a laser pulse was determined using an ablation curve. The fluence was varied from 40 mJ cm^{-2} to 420 mJ cm^{-2} with etch rate per pulse data calculated at each instance.

Figure 7 shows a comparison of experimental data to modelled data for the purpose of prediction model validation. Figure 7a presents a difference plot representing modelled and experimentally obtained values for ablated

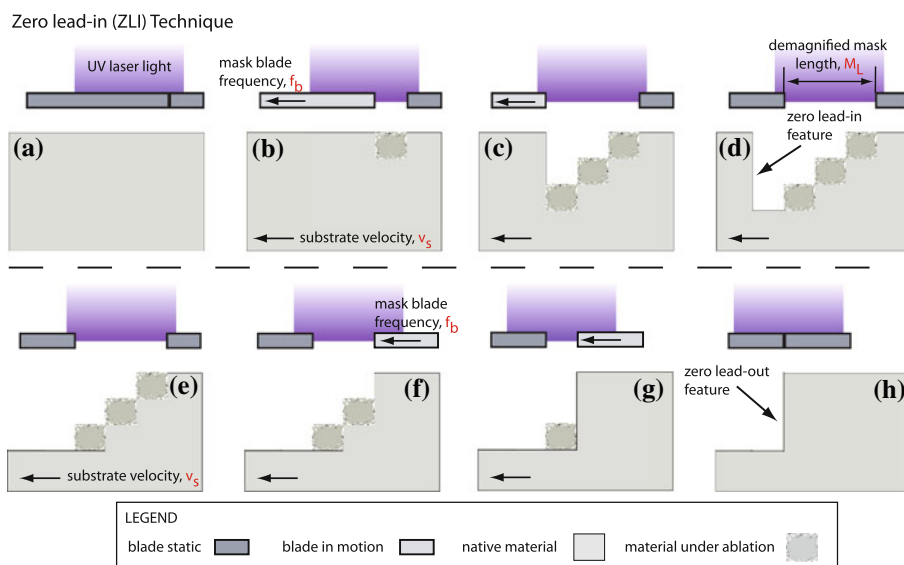


Fig. 4 Schematic diagram depicting the use of the IPM and ZLI technique to create a ramp free entrance (a–d), and exit (e–h), to a microchannel. For simplicity each shaded block with *material under ablation* represents a single laser pulse. **a** Initially, the blades are closed and the substrate is static. **b** The substrate and the leading IPM blade begin to move in unison at a velocity, v . **c** The lead-in ramp that would normally form begins to be eliminated. **d** The IPM blade stops

while the substrate continues moving. The result is a ZLI feature at the entrance to the microchannel. **e** The process begins with a lead-out ramp and static mask. **f** The trailing IPM blade begins to move in unison with the substrate at a velocity, v . **g** The lead-out ramp starts to be eliminated. **h** The final zero lead-out feature at the exit to the microchannel

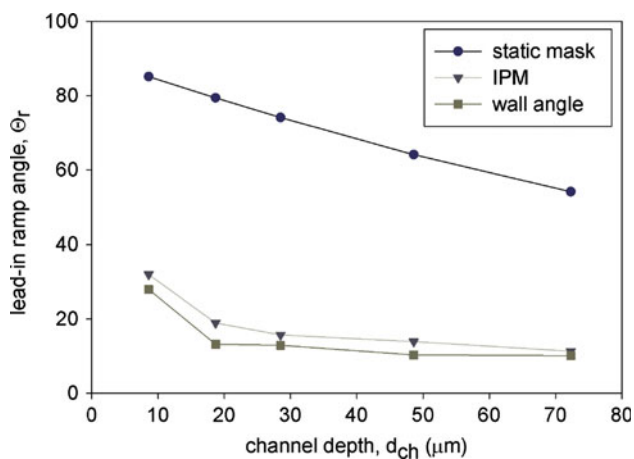


Fig. 5 Comparison of ramp angle, θ_r , for microchannels machined with a static mask and IPM using the ZLI technique as the velocity of the substrate is varied from 10 to 50 $\mu\text{m s}^{-1}$. For reference the cross-sectional sidewall angle of the microchannel is also included

periodic structures. By varying v_s and f_b , structures such as those in Fig. 8 were produced. To benchmark the model the period of these structures was measured and compared to the modelled data. The mean difference between the two data sets is 1.27 μm with a standard deviation of 1.7 μm . Figure 7b shows a difference plot representing modelled and experimental microchannel depth measurements. Channels were ablated at a constant v_s and f , 20 $\mu\text{m s}^{-1}$ and 50 Hz, respectively. The laser fluence, ϕ , and number

of pulses per area, NP_x , were varied to produce channels of varying depth for measurement. At a constant v_s and f , the NP_x was varied by adjusting the M_L . The mean difference between the two data sets is 2.08 μm with a standard deviation of 1.38 μm . Figure 7c shows the difference in measured microchannel width, w_{ch} , as the demagnification ratio of the laser system is varied. The mean difference in w_{ch} between the model and experimental data is 0.37 μm with a standard error in the mean (σ_M) of 0.10 μm . The small error makes it difficult to distinguish between the two data sets on the graph. These results give a good indication as to the accuracy of the prediction model. The next section looks at using the IPM, ZLI technique and prediction model to generate geometries for use as micromixers.

3.3 Micromixer geometries

The main aim of this work was not to produce new microfluidic mixing structures rather demonstrate a new technique for the production of such geometries. However, as a demonstration of the potential application of the IPM some structures are demonstrated whose fabrication is greatly simplified by use of the IPM. For a comprehensive review of various micromixing geometries found in the literature the reader is directed towards Nguyen and Wu (2005). The prediction model was used to generate three microchannel geometries of varying periodicity. Figure 8a shows the resulting geometries when a triangular waveform

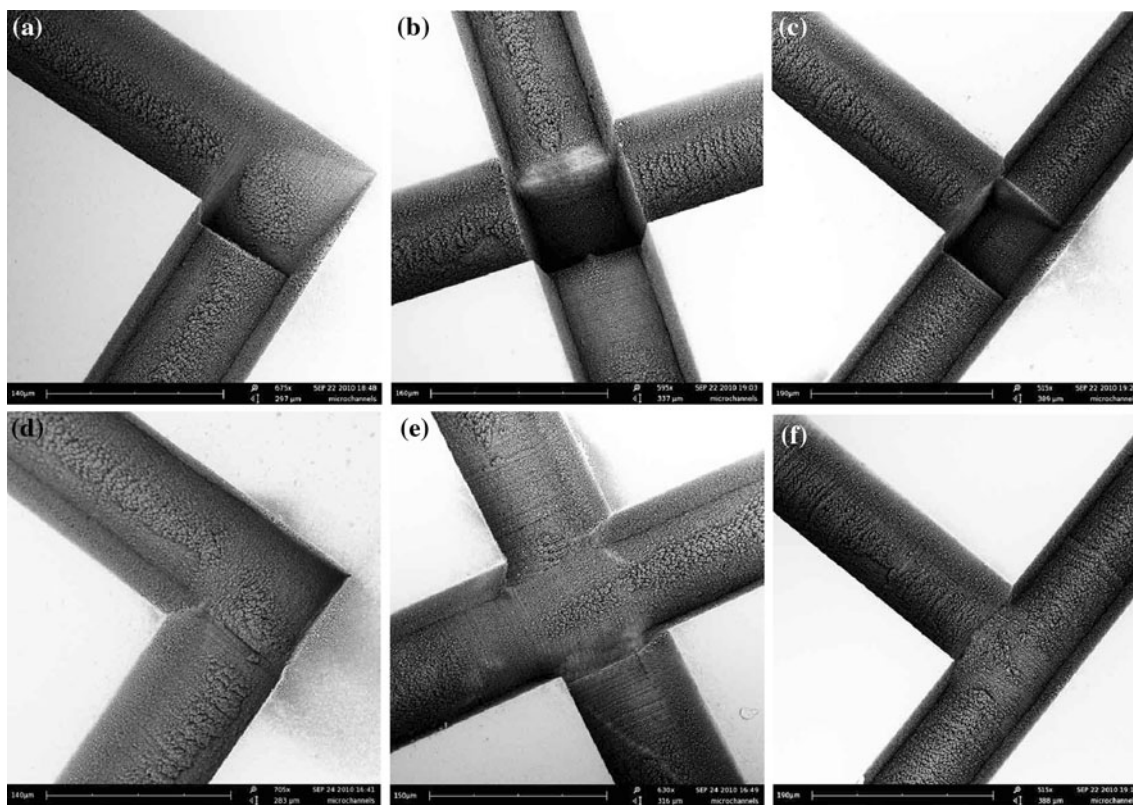


Fig. 6 Comparative SEM images of 100 μm × 50 μm channels created using scanning laser ablation through a static mask (a–c) and using the IPM employing the ZLI technique (d–f). **a** An over-etched junction (scale bar 140 μm). **b** A crossing channel with uniform over-

etched intersection (scale bar 160 μm). **c** An inlet channel with non-uniform over-etched intersection (scale bar 190 μm). **d** (scale bar 140 μm), **e** (scale bar 150 μm) and **f** (scale bar 190 μm) flat junctions produced with the IPM mask using the ZLI technique

was applied to the blade-pair perpendicular to the direction of motion of the X/Y stage. f_b is varied between 0.08, 0.16 and 0.32 Hz for the channels shown with the second blade pair set to a static, demagnified, opening of 40 μm. The channels were ablated with $f = 50$ Hz, $\phi = 250$ mJ cm⁻² and $v_s = 20$ μm ms⁻¹.

These geometries were then investigated using CFD techniques to assess their potential as microfluidic mixers. The three geometries modelled contained periodic elements of 400, 200 and 100 μm in length. The structures were approximated to be planar in nature so the analysis was carried out in 2D. The width of the microchannel, w_{ch} , in all cases was 100 μm with a gap width, w_g , of 20 μm—Fig. 8b. In order to assess the mixing performance, the micromixing geometries were included in a two-input microchannel. The concentration of species at inlet one and two was normalised to 0 and 1, respectively. Uniform mixing is achieved when the molar intensities of the two species reaches 0.5. To quantify the degree of mixing, the standard deviation of the intensity at each pixel in a channel cross-sectional is measured

$$\sigma = \left\langle (I - \langle I \rangle)^2 \right\rangle^{1/2} \tag{7}$$

here I is the pixel value (between 0 and 1), and $\langle I \rangle$ is the average over all the pixels in the cross-section (Stroock et al. 2002). The resulting value of σ will lie between 0 and 0.5, the latter representing completely segregated streams while the former fully mixed streams.

Figure 9a shows the results of simulations performed at a Reynolds number (Re) of 0.1. Cross-sectional concentration profiles were taken at various points along the channel to measure the development in mixing. It was found that all three mixing geometries result in similar levels of performance. Complete mixing was achieved after 1.5 cm in the structured microchannels while it takes 3 cm to mix in a plane microchannel. The longer periodic structure, 400 μm was found to have the lowest pressure drop. It out-performed the 200 μm and 100 μm structures by 10% and 50%, respectively. The effect of changing the type of waveform applied to the microchannels was also investigated. The profile of the channel was varied between a triangle, sawtooth (forward), sawtooth (reverse) and sine wave by adjusting the settings in the prediction model—example in Fig. 8b. The periodicity of the elements was set at 400 μm and the channels were modelled using the same parameters as the previous simulations. Figure 9b presents

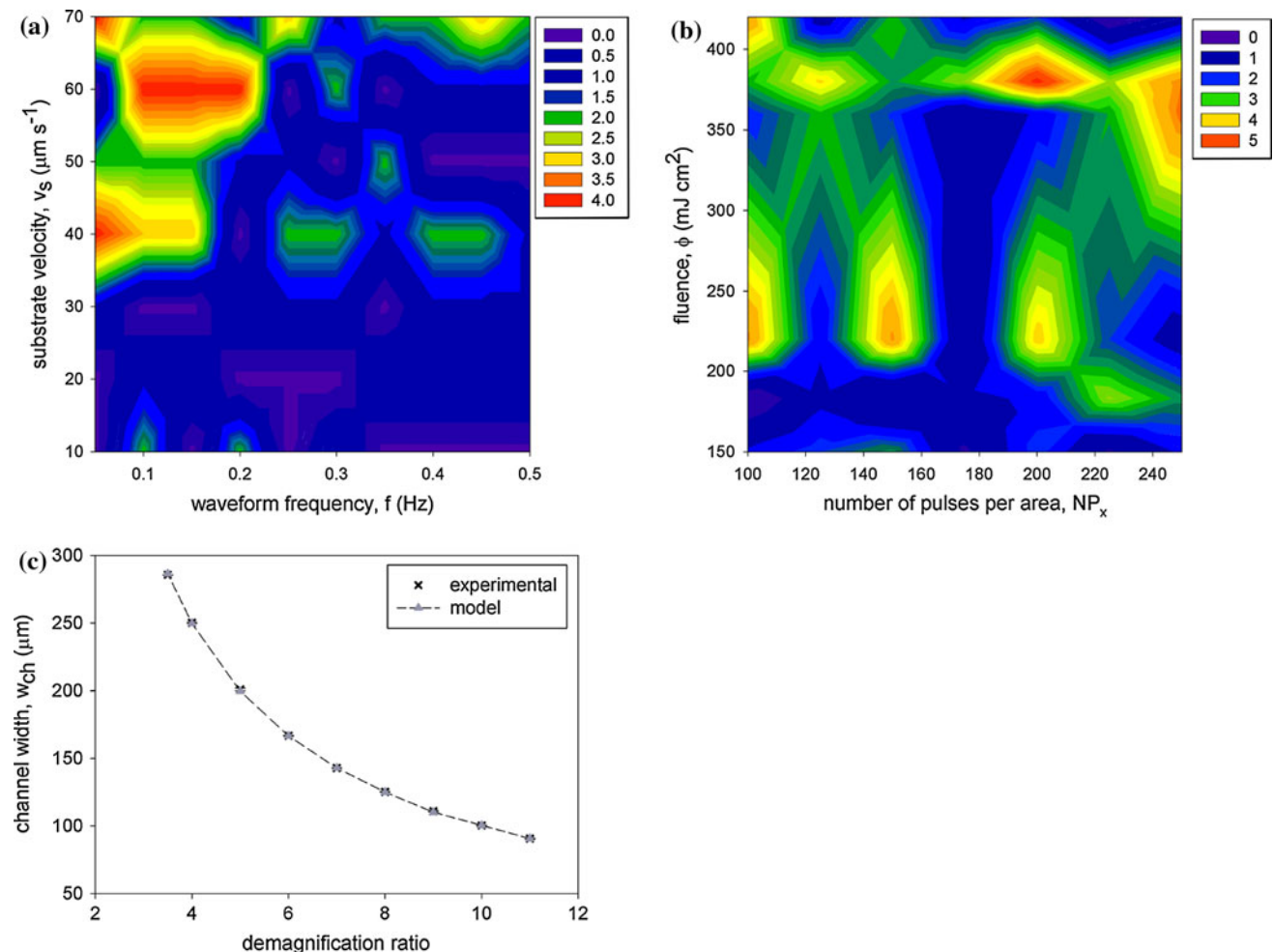


Fig. 7 Data depicting the difference between modelled and experimentally measured structures. **a** Difference plot for periodicity of ablated geometries related to mask blade frequency, f_b , and substrate velocity, v_s , ($\mu = 1.27 \mu\text{m}$, $\sigma = 1.17 \mu\text{m}$). **b** Difference plot for microchannel depth as a function of fluence, ϕ , and number of pulses per area, NP_x , ($\mu = 2.08 \mu\text{m}$, $\sigma = 1.38 \mu\text{m}$). **c** Comparison of the

channel width, w_{ch} , as the demagnification ratio is varied. ($\mu = 0.37 \mu\text{m}$, $\sigma_M = 0.10 \mu\text{m}$) (both data-sets overlap on the graph and the error bars associated with the experimental data are smaller than the graphed points). The scales in **a** and **b** represent difference in microns

the results of the simulations run at a Re of 0.1. The performance of the four geometries is similar with mixing achieved after 1.5 cm. The triangle waveform was found to have a marginally lower pressure drop ($\sim 10\%$) in comparison to the other three structures. At this Re diffusion is the dominant mixing process. This is aided by the focus-and-diverge effect created by the microchannel geometry. The similar performance seen across all channels may also be explained by this effect. In the microchannels with the shorter period features the flow does not get the opportunity to diverge sufficiently before coming into contact with the next focusing element. To improve the mixing over a wider range of Re will require specific tailoring of the mixing channel. This will come in the form of additional 2.5D and 3D obstacles within the channel.

4 Conclusions

A technique for the fabrication of microchannels in PMMA substrates using an excimer laser and IPM was presented. The demonstrated technique removes some of the complexity associated with producing microfluidic structures with excimer lasers and scanning laser ablation. Zero lead-in features have been shown to join microchannels with flat junctions. Channel geometry can be varied by changing the mask parameters during processing rather than switching between different masks, thus, greatly reducing the complexity of fabricating non-uniform microchannels using laser machining. A prediction model that accurately represents the machining process was described as a tool for microchannel development and refinement prior to the

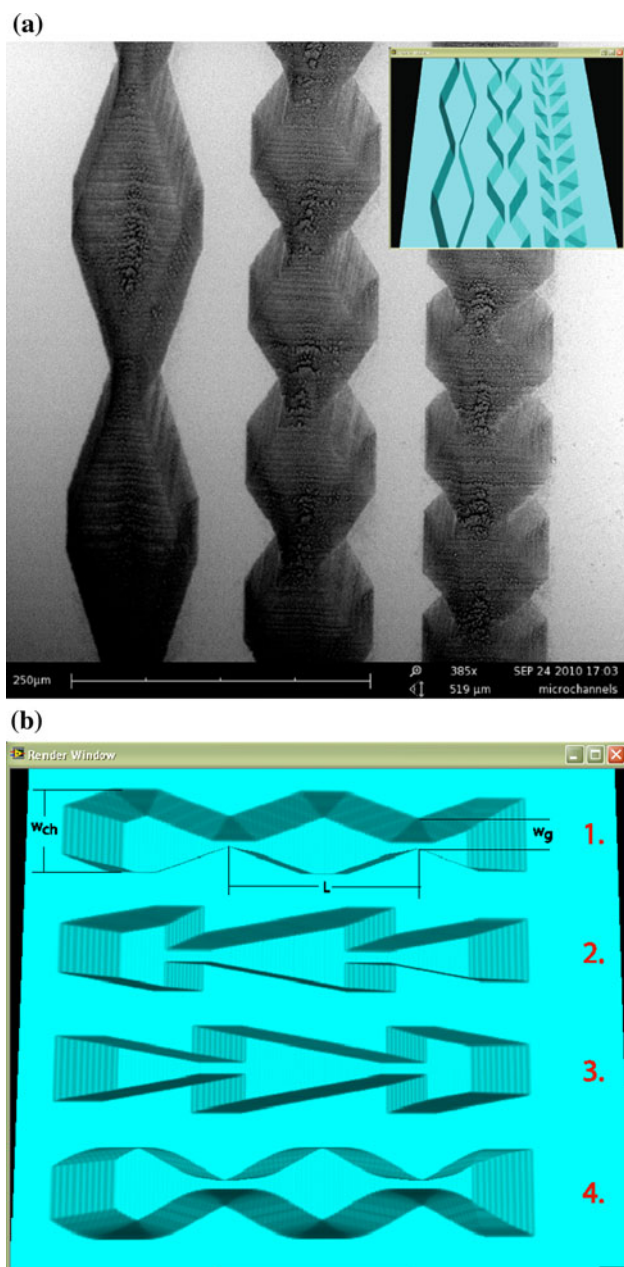


Fig. 8 **a** SEM image of fabricated structures on PMMA (scale bar 250 μm) (inset: simulated geometry from prediction model). **b** Simulated channels with varying periodic elements. 1 Triangle, 2 Sawtooth (forward), 3 Sawtooth (reverse), 4 Sine. The length of the periodic elements (L), the width of the channel (w_{ch}), and width of the gap (w_g) are all indicated

fabrication step. Model validation data showed good agreement between the model and experimental data. The effect of varying the overall channel geometry was explored using the prediction model and CFD analysis. It was found that applying a waveform to the channel edges improved the mixing efficiency of the microchannel by 50% in comparison to a standard straight channel. Future work will centre on the use of the prediction model to develop more complex

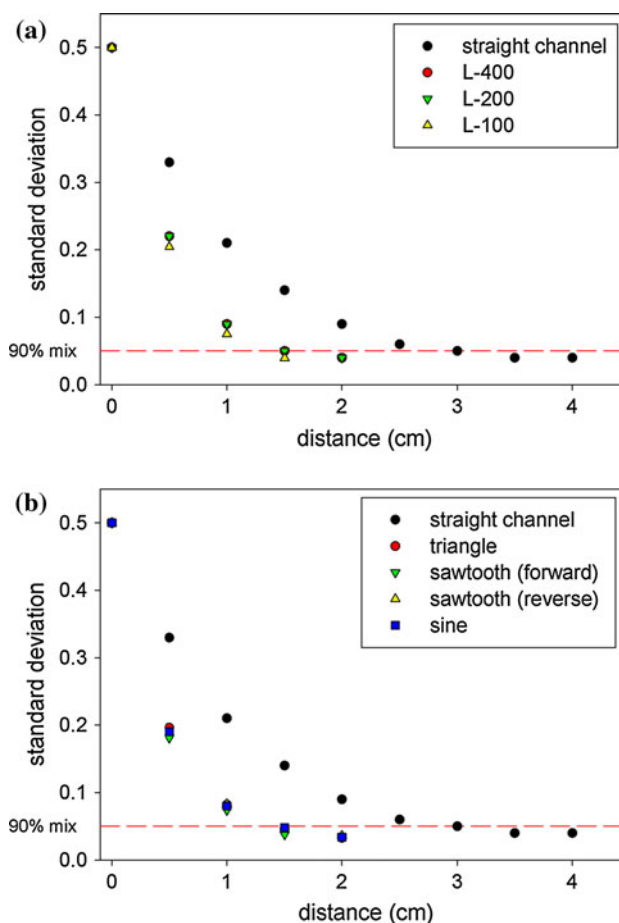


Fig. 9 Standard deviation of the output concentration profile of simulated microchannels. **a** Comparison of a straight channel to channels with a triangular profile of varying periodicity, and **b** comparison of straight channel to channels with various profiles: triangular, sawtooth (forward), sawtooth (reverse) and sine

mixing geometries with greater performance. Validation of the resulting geometries will be carried out over a wider range of Reynolds numbers to full quantify their performance. CFD analysis will be verified by the fabrication and subsequent testing of the mixing structures in the laboratory.

Acknowledgments This work was conducted under the framework of the INSPIRE programme, funded by the Irish Government’s Programme for Research in Third Level Institutions, Cycle 4, National Development Plan 2007-2013. It was supported by the NUI, Galway Science Faculty Fellowship and Enterprise Ireland Grant: CFTD/2005/309. The authors wish to acknowledge the Centre for Astronomy HPC for computational support, and extend their gratitude to the EPFL, and in particular, Sebastian Favre, Theo Lasser, Antonio Lopez, Thomas Sidler and Ronald Gianotti, for providing the prototype adjustable pinhole used in this work.

References

Abdelgawad M, Watson M, Young E, Mudrik J, Ungrin M, Wheeler A (2008) Soft lithography: masters on demand. Lab Chip 8:1379–1385

- Becker H, Gartner C (2008) Polymer microfabrication technologies for microfluidic systems. *Anal Bioanal Chem* 390:89–111
- Bhagat A, Peterson E, Papautsky I (2007) A passive planar micromixer with obstructions for mixing at low reynolds numbers. *JMM* 17:1017–1024
- Chong A, Jin-Woo C (2004) Springer handbook of nanotechnology. Springer, New York
- Chung C, Shih T (2008) Effect of geometry on fluid mixing of the rhombic micromixers. *Microfluid Nanofluid* 4:419–425
- Gower MC (1999) Excimer laser micromachining: a 15-year perspective. In: Proceedings of laser applications in microelectronic and optoelectronic manufacturing IV, vol 3618, San Jose, CA, USA, pp 251–261. SPIE
- Heng Q, Tao C, Tie-chuan Z (2006) Surface roughness analysis and improvement of micro-fluidic channel with excimer laser. *Microfluid Nanofluid* 2:357–360
- Hong TF, Ju WJ, Wu MC, Tai CH, Tsai CH, Fu LM (2010) Rapid prototyping of pmma microfluidic chips utilizing a CO₂ laser. *Microfluid Nanofluid* 9(6):1125–1133
- Khan Malek C (2006a) Laser processing for bio-microfluidics applications (part I). *Anal Bioanal Chem* 385:1351–1361
- Khan Malek C (2006b) Laser processing for bio-microfluidics applications (part II). *Anal Bioanal Chem* 385:1362–1369
- Klank H, Kutter J, Geschke O (2002) CO₂-laser micromachining and back-end processing for rapid production of pmma-based microfluidic systems. *Lab Chip* 2:242–246
- Li C, Yang J, Tzang C, Zhao J, Yang M (2006) Using thermally printed transparency as photomasks to generate microfluidic structures in pdms material. *Sens Actuators A* 126:463–468
- Lim D, Kamotani Y, Cho B, Mazumder J, Takayama S (2003) Fabrication of microfluidic mixers and artificial vasculatures using a high-brightness diode-pumped Nd:YAG laser direct write method. *Lab Chip* 3:318–323
- Liu A, He F, Wang K, Zhou T, Lu Y, Xia X (2005) Rapid method for design and fabrication of passive micromixers in microfluidic devices using a direct-printing process. *Lab Chip* 5:974–978
- Lucio do Lago C, Torres da Silva H, Neves C, Alves Brito-Neto J, Fracassi da Silva J (2003) A dry process for production of microfluidic devices based on the lamination of laser-printed polyester films. *Anal Chem* 75:3853–3858
- Nguyen NT, Wu Z (2005) Micromixers—a review. *J Micromech Microeng* 15(2):R1
- Pfleging W, Kohler R, Schierjott P, Hoffmann W (2009) Laser patterning and packaging of CCD-CE-chips made of pmma. *Sens Actuators B* 138:336–343
- Rizvi NH (1999) Production of novel 3d microstructures using excimer laser mask projection techniques. In: Proceedings of design, test, and microfabrication of MEMS and MOEMS, vol 3680, Paris, France, pp 546–552. SPIE
- Roberts M, Rossier J, Bercier P, Girault H (1997) Uv laser machined polymer substrates for the development of microdiagnostic systems. *Anal Chem* 69:2035–2042
- Shih T, Chung C (2007) A high-efficiency planar micromixer with convection and diffusion mixing over a wide reynolds number range. *Microfluid Nanofluid* 5(2):175–183
- Shim J, Nikcevic I, Rust M, Bhagat A, Heineman W, Seliskar C, Ahn C, Papautsky I (2007) Simple passive micromixer using recombinant multiple flow streams. In: Proceedings of microfluidics, BioMEMS, and medical microsystems, V, vol 6465, p 64650Y. SPIE
- Sidler T, Favre S, Lopez A, Gianotti R, Lasser T, Wolleschensky R (2004) Intelligent pinhole with sub-micrometer resolution. In: Proceedings of the 13th international conference on microoptics (MOC'04), Jena, Germany
- Stroock A, Dertinger S, Ajdari A, Mezic I, Stone H, Whitesides G (2002) Chaotic mixer for microchannels. *Science* 295:647–651
- Tan A, Rodgers K, Murrilhy J, OMathuna C, Glennon J (2001) Rapid fabrication of microfluidic devices in poly(dimethylsiloxane) by photocopying. *Lab Chip* 1:7–9
- Waddell E, Locascio L, Kramer G (2002) Uv laser micromachining of polymers for microfluidic applications. *ALA* 7:78–82
- Yoshida Y (2007) Fabrication of bio-chips by laser ablation. In: Proceedings of photon processing in microelectronics and photonics VI, vol 6458, p 64580A–8 San Jose, CA, USA. SPIE